Fractal viscous fingering in inhomogeneous porous models

U. Oxaal
Department of Physics, University of Oslo, Box 1048, Blindern, 0136 Oslo 3, Norway
(Received 15 March 1991; revised manuscript received 17 July 1991)

Immiscible fluid-fluid displacement was studied experimentally and numerically in porous models consisting of uniform pores on a square lattice where all nearest neighbors were connected by bonds randomly given one of two permeabilities. Patterns formed by a high-viscosity fluid (glycerol) being displaced by a low-viscosity fluid (air) injected at the center of the model network were studied and compared with the results of diffusion-limited-aggregation (DLA) simulations using a network with identical geometry. For a bond permeability ratio $\kappa \simeq 0.004$ close to the bond percolation threshold $f_c = 0.5$ of high-permeability bonds, simulated and experimental patterns exhibit a high degree of overlap. The displacement patterns generated in experiments and in simulations can be characterized by the same effective fractal dimension $D_c \simeq 1.5$. We find that the model geometry strongly influences the structure of the displacement pattern formed, and that Meakin *et al.*'s [Physica A **115**, 1 (1989)] modified-DLA algorithm provides a good model for the displacement.

PACS number(s): 47.55.Mh, 47.55.Kf, 64.60.Ak, 05.40.+j

I. INTRODUCTION

Complicated patterns arise in many flow situations. Clouds formed during turbulent flow of air and the structures observed in convective flows are well-known examples. During the displacement of one fluid by another in porous media, fronts are formed. These fronts often have complicated structures. Depending on the displacement rate, viscosity ratio, miscibility, interfacial tensions, and pore geometry, a variety of displacement patterns arise. In the pattern formation, the disorder of the porous matrix plays a key role that is not well understood.

Fractal [1] displacement fronts have been observed both during slow and fast displacement [2,3].

Viscous fingering (VF) refers to the onset and growth of instabilities in the displacement fronts that arise when a low-viscosity fluid (1) quickly displaces a high-viscosity fluid (2) ($\mu_1 \ll \mu_2$). In a homogeneous porous medium, when the displaced fluid wets the solid matrix, fractal patterns are observed [4–6]. When the displacement is fast, the capillary number, defined by $\mathrm{Ca} = \mu U/\sigma$, is large. Here μ is the viscosity of the displaced fluid, U is the average front velocity, and σ is the surface tension between the two fluids. This dimensionless parameter relates the strength of long-range viscous forces to local capillary forces. Viscous forces dominate at high displacement rates, at values of $\mathrm{Ca} \simeq 0.02$ or above [6].

Viscous flow of a fluid in a porous medium is described by Darcy's law, which, neglecting gravity effects, may be written

$$\mathbf{v} = -\frac{k}{\mu}\nabla P \ , \tag{1}$$

where $\mathbf{v}$ is the average fluid velocity, ∇P and μ are, respectively, the pressure gradient and viscosity of the fluid, and k the average permeability of the medium. For incompressible fluids $\nabla \cdot \mathbf{v} = 0$ and therefore

$$\nabla \cdot (k \nabla P) = 0 \ . \tag{2}$$

If the permeability k is constant, (2) reduces to the Laplace equation

$$\nabla^2 P = 0 \ . \tag{3}$$

When one fluid is displaced by another, the description of fluid flow is more complex. In traditional reservoir simulations [7] one introduces a Darcy equation similar to (1) for each fluid component i:

$$\mathbf{v}_i = -\frac{k k_{ri}}{\mu_i}\nabla P_i \ , \tag{4}$$

where the *phenomenological* relative permeability of the ith fluid, k_{ri}, depends on the relative amounts of fluids in the pore space. However, the very concept of relative permeabilities is inapplicable for nonstationary situations and, in this simple form, incorrect for even the simplest capillary tube experiments [8].

However, the patterns generated in a fluid-fluid displacement experiment in a two-dimensional porous model [5,9–11] are similar to the patterns generated by the diffusion-limited-aggregation (DLA) algorithm [12] (see Sec. IV A), the dielectric breakdown models, and discrete solutions of the Laplace equation [13]. Simulated DLA patterns and experimental observations *look* much the same and have similar fractal dimensions.

The DLA model of Witten and Sander [12] is a general, stochastic model without details specific to the physics of two-fluid displacement in porous media. It is simple and fast compared to numeric solutions of the flow equations in network models.

The aim of this paper is to test in detail to what extent two-phase flow *in a complex porous model* may be modeled by the simple extension of the DLA algorithm described by Meakin *et al.* [14].

To do this we make model porous media with a known

but complicated pore-space geometry based on percolation theory. Percolation clusters have nontrivial geometries that are completely characterized in a statistical sense, and we use them as basis for our model porous media.

In previous experiments on porous models at the percolation threshold by Oxaal *et al.* [15], we used models consisting of pores on a square lattice randomly connected by bonds between nearest-neighbor pores. The fraction of bonds was at the threshold for bond percolation on a square lattice, which is $f_c=0.50$. Connected pores form clusters, and flow was possible only on the spanning cluster, i.e., on the pores all strung together in a connected labyrinth that contained both the central site (where the displacing fluid was injected) *and* was connected to the boundary (where the displaced fluid was expelled). Incompressible fluid flow is confined to the backbone of the spanning cluster since the invading fluid cannot enter the dead ends. Experiments agreed with simulations solving a discretized Laplace equation [16,17] for fast displacement and with the so-called $\eta\rightarrow 0$ model for slow rates. By itself, the geometric restriction of the backbone favors high correspondence between experiment and simulation.

Real porous media are seldom exactly at the percolation threshold, and so we consider departures from critical percolation. There are two ways of doing this: We may increase the fraction of bonds above f_c or we may add weak bonds where previously none were present. These two ingredients may be mixed.

Adding low-permeability bonds where previously none were present introduces a new length scale [14] in the pore-space geometry (see Sec. II B), which in turn may influence the fluid-displacement process. The patterns formed change, since the low-permeability bonds make "would-be" dead ends available and also permit flow of fluid in finite clusters of high-permeability bonds. The displacement patterns also scale differently on various length scales. To know the relevant scaling relations and the length scales where they apply is important in applications such as oil recovery, besides being interesting from a physical point of view.

The type of network we describe in this paper may map onto macroscopic situations like regions of high-permeability rock embedded in low-permeability rock or fractured (low-permeability) rock.

In Secs. II A and II B we describe the random geometry of the model and scaling relations for aggregates formed on the model. We give a detailed description of the experiment and data collection in Sec. III. The algorithm used in the simulations is described in Sec. IV B, and in Sec. V we present experimental and numerical results. Section VI contains discussion and conclusions.

II. GEOMETRY

A. Model geometry

We made models consisting of cylindrical pores connected by bonds between nearest neighbors on a 145×145 square lattice. Each bond was randomly given one of two permeabilities: a fixed high value, which we set equal to one, and a lower value $\kappa=4\times 10^{-3}$. The fraction of high-permeability bonds in the model was $f=0.497$, close to the critical value for bond percolation on a square lattice, $f_c=0.50$. The fraction of low-permeability bonds was $1-f=0.503$. Figure 1(a) shows a small part of our model.

In bond percolation, where bonds are present or absent with probabilities f and $1-f$, we define *clusters* as groups of pores (or lattice sites) connected by bonds. In the present case we define clusters to be groups of pores connected by *high-permeability* bonds. These definitions are equivalent if we for a moment ignore the existence of low-permeability bonds. One high-permeability bond connecting two pores (sites) will be called a cluster of size 2, and s pores in some way connected by high-permeability bonds will be called a cluster of size s.

A cluster has a characteristic size that may be given by

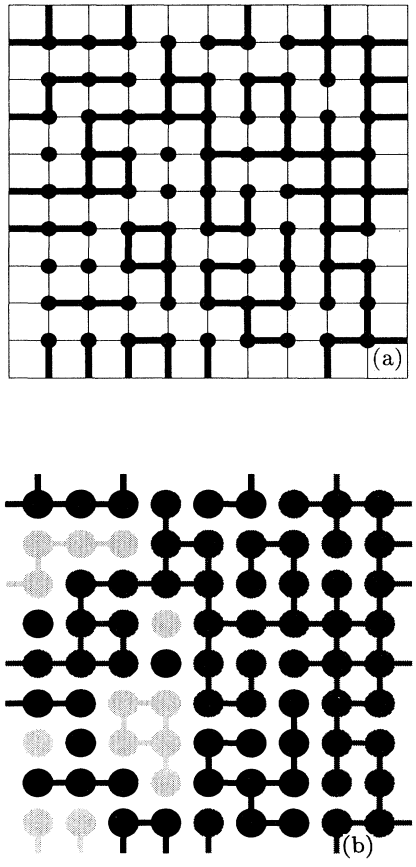

FIG. 1. (a) Enlarged portion of the model showing pores connected by high- or low-permeability bonds between nearest neighbors. (b) The same portion of the model showing different clusters of pores connected by high-permeability bonds in shades of gray. The color of pores and high-permeability bonds specify the cluster that they are part of, while low-permeability bonds and matrix appear as white background.

its radius of gyration:

$$R_g=\left[\frac{1}{s}\sum_{i=1}^{s}|\mathbf{r}_i-\mathbf{r}_0|^2\right]^{1/2}, \tag{5}$$

where $\mathbf{r}_i$ is the position of the ith pore in the cluster, s is the cluster size, and $\mathbf{r}_0$ is the position of the center of mass, given by

$$\mathbf{r}_0=\frac{1}{s}\sum_{i=1}^{s}\mathbf{r}_i . \tag{6}$$

To characterize a given model we define a local correlation length ξ as an average distance between two pores connected through high-permeability bonds:

$$\xi^2=\frac{\sum_j R_g^2(j)s_j^2 n_j}{\sum_j s_j^2 n_j}, \tag{7}$$

where s_j and $R_g(j)$ are the number of pores and radius of gyration of cluster j and n_j is the probability per pore to belong to that cluster. The sum runs over all clusters in the model also those including pores at the boundary. We chose to include them since we focused on the structure formed by clusters of pores that we expected to dominate the fluid transport from the center to the boundary, and many of the largest clusters include pores at the boundary. However, note that clusters that include boundary sites are usually discarded, since they are truncated by the boundary and their shape as expressed by R_g is not representative. The local correlation length of our experimental model was $\xi=25.4$ lattice constants.

B. Scaling and crossover

When air injected at the center displaces viscous fluid from the model, we may at any instance t count the number of drained pores. Since we associate a constant amount of fluid with each pore, the cluster of drained pores represents a certain mass $M(t)$. The empty pores are all connected by drained bonds of either kind and form an aggregate. We calculate the radius of gyration $R_g(t)$ of the aggregate around its center of injection instead of its center of mass when using Eq. (5).

We find that the mass $M(t)$ increases with the radius of gyration $R_g(t)$ to some power D_g,

$$M\sim R_g^{D_g} . \tag{8}$$

The exponent D_g is called the *radius of gyration dimension* [18], and it is a noninteger number less than the spatial dimension $d=2$.

The above relation is a common way of characterizing the scaling behavior of DLA clusters. It compares the mass M and radius of gyration R_g of different structures, such as stages of an experiment of a simulation.

Another common way of finding a fractal dimension of a radially grown aggregate is to measure the cumulative mass $M(R)$ of an aggregate within circles of successively increasing radius R centered at the site of injection (or seed particle). This function is easy to measure and gives a robust measure of the scaling property of a *given* structure. The aggregate reaches its total mass M_0 at the maximum radius R_0 proportional to R_g. The scaling of $M(R)$ is given by

$$M(R)/M_0=(R/R_g)^{D_c}F(R/R_g) . \tag{9}$$

Here M_0 is the total cluster mass, D_c the *cluster dimension,* and $F(x)$ describes the crossover. We scale the circle radius with R_g rather than with R_0, since R_g is less sensitive to fluctuations in the aggregate shape.

For structures scaling with an exponent D_c, $F(x)$ is constant in the range $x<1$ and tends to x^{-D_c} for $x>1$, so that $M\to M_0$ as $R\gg R_g$.

Different ways of presenting the same data emphasize various aspects of the results. The exponent D_g characterizes the scaling of a developing structure, whereas the exponent D_c only describes the geometric scaling of the last stage. In Sec. VI we discuss how the two exponents are related.

Based on simulations, Meakin *et al.* [14] describe the dependence of the aggregate mass M on length R by the scaling form

$$M(R)\sim R^{D_2}G(R/\xi,R/L_\kappa) . \tag{10}$$

The exponent $D_2=1.3$ is the fractal dimension associated with DLA on an infinite cluster at the percolation threshold [15,17], $\xi\sim(f-f_c)^{-\nu}$ is the usual correlation length as a function of the fraction f of high-permeability bonds, f_c is the percolation threshold fraction of bonds on a square lattice, and $\nu=\frac{4}{3}$ is the correlation length exponent [19]. L_κ is a length set by the bond permeability ratio κ through

$$L_\kappa\sim\kappa^{-\alpha} , \tag{11}$$

where α is a crossover exponent. $G(x,y)$ is a crossover function that describes how the scaling relation changes from that of DLA on a percolation cluster at f_c to that of DLA on a homogeneous model as the pore space changes from a percolative geometry to a uniform one by an increase in κ or f or both.

Meakin *et al.* [14] discuss the form of $G(x,y)$ in some limiting cases: As $\kappa\to 0$, the length scale $L_\kappa\to\infty$, and for $f=f_c$ this yields the scaling of DLA on a percolation cluster [15,17] $M\sim R^{D_2}$, with $D_2=1.3$. As the fraction f of high-permeability bonds changes away from f_c, the correlation length ξ decreases and will eventually become less than the model size L. On length scales $R<\xi$, the aggregate mass will scale as if on a percolation cluster with an exponent $D_2=1.3$, whereas the model will be homogeneous at length scales $R>\xi$ and aggregate mass should scale with length to a power $D_1=1.7$. Thus, provided $\kappa\ll 1$ and ξ is in the range $a<\xi<R_g<L$, a crossover in scaling of M as function of size from $D_2=1.3$ to $D_1=1.7$ is expected to be observed.

As the permeability ratio κ increases, the associated length L_κ decreases, i.e., the contribution from low-

permeability bonds to transport properties of the model increases. As $\kappa \to 1$, the scaling behavior of the homogeneous model $M \sim R^{D_1}$ with $D_1 = 1.7$ should be observed independent of f.

The scaling and crossover behavior when both ξ and L_κ have intermediate values compared to the model size L has not been discussed, but is expected to be complicated. It is also a region of expected practical importance, since naturally occurring porous media are homogeneous above and inhomogeneous below certain length scales and may have permeability ratios anywhere in the range [0,1].

III. EXPERIMENT

Physical models were made by a photolithographic technique using a computer-generated transparent mask to prevent uv-polymerization in designated areas of the photosensitive nylon layer of a printing plate. After uv exposure the unpolymerized nylon was washed away, and we obtained a recessed pattern of pores connected by bonds. A "lid" was clamped over the pattern, and we obtained a network where fluid flow was only possible on the etched network. The network was filled with dyed glycerol, later displaced by air injected at the center. The setup permitted the displacement process to be photographed from above. The photographs were digitized, and we were able to find the coordinates of the drained pores in the aggregate and relate these data to the cluster structure of the model. Once the coordinates of the experimentally obtained aggregate where known, we could find the scaling relations and, in detail, compare experimental with simulated aggregates.

In the following subsections we give a detailed description of the experimental method.

A. Design of pattern

We chose a design, shown in Fig. 1(a), with a fixed pore diameter d equal to one-half of the lattice constant a and a fixed bond length of $a/2$. The high-permeability bonds have a width W and the low-permeability bonds a width w. The large pores facilitate digitization of the experiment (see Sec. III E).

The technique we use to make the photolithographic mask limits the resolution we may achieve. Ideally, we want a model with infinitesimally thin low-permeability bonds. However, even a "large" ratio such as $\kappa \simeq 10^{-8}$ requires a linewidth ratio $w/W = 0.01$ since the volume flux through a simple tube changes with its width to the fourth power. Using the lattice design of Fig. 1(a), we would get a lattice constant $a = 2d = 4W = 400w$. Thus the lattice design, permeability ratio, and linewidth resolution of drawing determine the lattice constant of the network. Our Tektronix 4693 printer could print a minimum line width of 84.6 μm. In practice, we must draw the thinnest bond at twice the printer resolution to prevent the processor in the printer from removing bonds as it rounds off values received from the computer. The low-permeability bonds would then have a width of 170 μm, yielding a lattice constant $a \simeq 68$ mm. The available printer paper would then permit a lattice of about 5×5 pores. Clearly, such lattices would be too small. Compromising, we used a ratio of bond widths, $w/W = 0.25$, giving a lattice constant $a = 2.7$ mm. The paper size then allowed a grid of 80×80 pores. The lattice size was increased to 145×145 pores by printing the pattern in four parts, assembling them, and reducing the grid photographically to fit the 310-mm-wide plate into which the pattern was etched.

It is possible to obtain a larger lattice by photographically decreasing the pattern more and by reducing the ratios d/W and a/d. With such models, however, the pressure needed to close the model (see Sec. III C) and the data acquisition (see Sec. III E) set experimental limits. The model we have used is close to the limit of what may be achieved using the experimental techniques of this paper.

B. Production of model

The assembled network was photographically reduced to 28.5×28.5 cm^2 onto Agfa Rapidoline Ortho RA716 pm film. The pores and bonds appeared in black, while the regions blocked to flow were transparent. The film was used to mask photosensitive nylon plate (BASF Nyloprint WA175) during exposure (14 min at a distance of 1 m from the lamps) to ultraviolet radiation from a Philips tabletop solarium (model HP3150/01A).

The unmasked portions of the plate were hardened by uv polymerization, while the regions masked by black remained unpolymerized, soft, and water soluble. After exposure unpolymerized nylon was removed with water under high pressure. The hardened regions remained, and pores and bonds formed a recessed pattern in the nylon plate.

Narrow bonds became more shallow than wide bonds because the uv light came in at angles between 0° and 22° to the surface normal. A simple geometric argument lets us approximate the depth of the bonds to be equal to their width. This was roughly what was observed using a stereoscopic microscope.

The bond widths of the finished model were measured under a Nikon SMZ-10 stereoscopic microscope with a ruler having divisions of 0.1 mm. The average bond widths were $w = 0.145 \pm 0.03$ mm and $W = 0.58 \pm 0.03$ mm, and the permeability ratio calculated with these values was $\kappa = (w/W)^4 \simeq 4 \times 10^{-3}$.

The nylon plate is red, and photographically this background provided poor contrast to fluids of almost any other color. We coated the models with an aluminum layer about 0.1 μm thick by vapor deposition. The color contrast to the dyed glycerol was thereby improved. In addition, it improved the wettability of the model surface toward glycerol.

C. Running an experiment

Figures 2 and 3 show the experimental arrangement. The model was sandwiched between two 15-mm Plexiglas plates held together by 12 clamps. The upper plate was clamped together with a 0.02-mm-thick Mylar membrane, and air at 3–5 kPa above the pressure on the

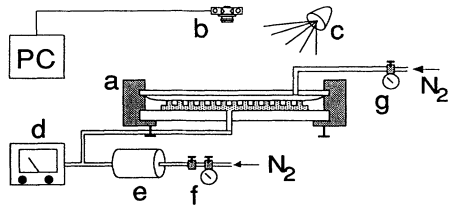

FIG. 2. Experimental setup. *a*, the model in its holder is shown in detail in the next figure *b*, camera; *c*, lamps; *d*, pressure gauge, *e*, buffer volume, *f*, pressure reduction system; and *g*, pressure to membrane.

displacing fluid was applied to the space between. Pressure on the membrane was controlled by a Norgren low-pressure valve and measured with a barometer (manometer). The applied pressure forced the Mylar membrane into contact with the etched side of the model as Fig. 3 shows, and so the flow of fluid was confined to the channels. Wide channels around and leading out of the boundary kept the model open to flow and the boundary pressure at ambient conditions. The plates and membrane were transparent, permitting photography from above.

Before the model was closed, a mixture of pure glycerol, water, and a black dye (water-soluble Nigrosine Merck "Certistain") was poured over the model. The viscosity was $\mu \simeq 380$ cP. The open model was placed in an evacuating chamber to remove air trapped in the pores. The model was closed by the inflated membrane as described above.

During experiments, air at constant pressure was injected from below through a 0.7-mm hole into the pore at the center of the model. Pressure of the injected air was measured differential to ambient conditions with a Texas Instrument fused-quartz pressure gauge. Pressure fluctuations at the center were typically less than 1%. As air intruded, a growing structure of air-filled pores and bonds was observed and photographed. When the intruding air reached the boundary of the model, the set pressure could not be maintained and the experiment was stopped. The displacement process was photographed from above using a Nikon F3 camera with 50-mm Nikkor lens and motordrive. We used Agfapan professional black-and-white 100 ASA film. The camera was triggered by an IBM PC that also recorded the moment at which each frame was taken. Lighting was provided from above by four halogen lamps.

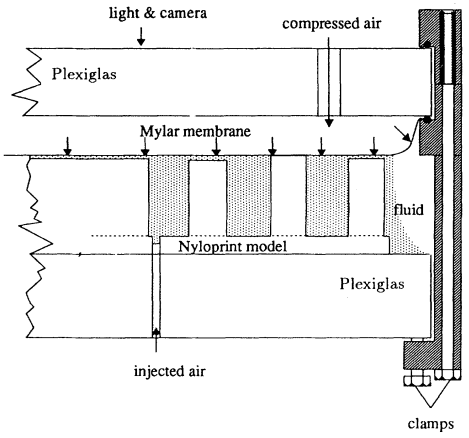

FIG. 3. Model consisting of a nylon printing plate (BASF), with a recessed network pattern on one side was closed by a Mylar membrane. The assembly was supported by 15-mm-thick Plexiglas plates held by clamps. The Mylar was kept in contact with the model by pressurized air as shown. The displacing phase was injected at the center, from below.

D. Displacement conditions

The maximum displacement pressure we used was 390 mbar above ambient conditions.

We determined the capillary number Ca, by finding the average front velocity U from a digitized sequence of photographs of the displacement experiment. Plotting the maximum cluster radius R_{max} versus t (Fig. 4), we found U in units of lattice constants per second from the linear fit. The maximum capillary number used in the experiments was $Ca \simeq 0.12$, and the minimum value we used was $Ca \simeq 0.02$. According to Lenormand, Touboul, and Zarcone [6], our experiments at $Ca = 0.03$ and above fall within the viscous-fingering domain, where viscous forces dominate and DLA is expected to be a valid model. Our experiments at $Ca \simeq 0.03$ and 0.02 are borderline cases, and we concentrate on the experiments at $Ca \simeq 0.12$.

We let the pressure on the membrane closing the model exceed the displacing pressure by about 10% to ensure that the membrane stayed in position during the displacement, and the maximum force on the plates holding the model was around 10^4 N. We have not explored at which applied pressure the unit bursts, but the pressure requirements grow inversely with the permeability of the model. In models of the present size, but having an increased lat-

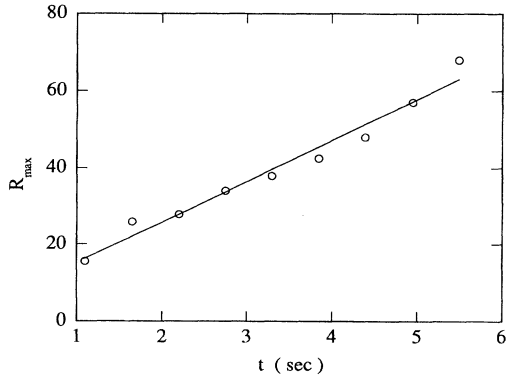

FIG. 4. Experiment. The largest cluster radius R_{max} vs time t for the experiment at $f \simeq 0.50$. The line shows a linear fit and a velocity $U = 10.7$ lattice constants per second is obtained from the fit.

tice resolution of 1000×1000 pores, pressure requirements would increase by a factor of 10^2-10^4 to reach a capillary number $Ca\simeq0.1$.

E. Digitization

To find quantities such as $M(t)$ and $R_g(t)$, we digitized the negatives obtained in experiments with a Nikon LS-3500 Film Scanner controlled from an Apollo DN4000 work station at a resolution of 4000×4000 pixels for each frame. The scanner resolves 256 levels of intensity in each pixel. The film scanner reads 35-mm film and the image area is 24 mm wide; i.e., the thinnest feature the scanner can resolve is 24 mm/4000=6 μm wide. This corresponds to a feature of 71.3 μm in our model. We measured thin bond widths around 150 μm, and this corresponds to one to two pixels in the digitized image.

We found the pores invaded by air in the following way: Before we started the flow of air, we took a picture of the filled model, where the network of channels appeared black on a white background. As air displaced the dyed glycerol, pores and bonds invaded by air appeared white as Fig. 5 shows. By numerically subtracting the first image from later frames, we obtained only the *differences* causes by the injected air; emptied pores and bonds appeared white on a dark background. By this procedure we acquired the pattern formed by the injected air, parts of which otherwise would be lost. The software allows correction for alignment errors between individual frames, for distortions of the grid by the lens, and for uneven lighting.

However, information about displacement in the low-permeability bonds was lost when subtracting, since we were unable to superimpose the two images to the required accuracy of one to two pixels. A main difficulty was to rotate the two images (numerically) to align the lattice axes exactly. Small deviations would cause the low-permeability bonds to literally black out.

Having placed the digitized image back onto the grid, we could identify the coordinates where air had entered. The total number of *pores* was underestimated by roughly 5% of the total number and the number of bonds even more. Since bonds were not reliably obtainable, we concentrated on the pores in the aggregate.

Now the experimental results could be compared with those of the simulations performed on exactly the same configuration of high- and low-permeability bonds, as well as with simulations on other models.

IV. SIMULATIONS

A. DLA algorithm

In the DLA model of Witten and Sander [12], particles are added, one at a time, to a growing aggregate. The simulation starts with a central fixed seed particle and another mobile particle at "infinity." This particle performs a random walk until it reaches a neighboring site of the seed. Here the particle terminates its random walk and becomes a permanently fixed part of the aggregate. The process is continued by starting new particles at infinity, one at a time. Each new particle walks until it reaches an empty neighbor site of any occupied site, where it is added to the growing aggregate.

The growth of the DLA aggregate is a stochastic process where the growth probability for a particle to hit (and stick to) the aggregate is given by the gradient of the probability field obeying the Laplace equation. The generated patterns occur with a probability proportional to their statistical weight. In all physical realizations of the DLA model, a random-growth process occurs in which the probabilities for growth are controlled by a field that obeys the Laplace equation. Paterson pointed out [9] that in viscous fingering the pressure field satisfies the Laplace equation and that DLA describes the process.

B. Meakin's modifications of the DLA algorithm

Our simulations are a modified version of ordinary DLA that take into account the permeability fluctuations of the porous model. This algorithm was introduced by Meakin *et al.* [14]. We used their computer program, and we follow their description closely.

The boundary conditions used correspond to those of the experiments we performed. The simulation started with single occupied site at the center of the model and was halted when a site at the boundary of the model was reached.

To represent the flow of viscous fluid through the network, a random walker moved with probabilities P_i along each of the four channels associated with its position on the lattice. Here $P_i=\kappa_i/\kappa_T$, where P_i and κ_i are the probabilities and permeabilities associated with the ith bond and κ_T is given by

$$\kappa_T=\sum_{i=1}^{4}\kappa_i \ . \tag{12}$$

The probabilities P_i $(i=1,2,3,4)$ were calculated for each lattice site before the simulation began, based on a list of coordinates for high- and low-permeability bonds. "Simulations on the experimental model" refers to use of the list of coordinates we used when we made the nylon model and the same permeability ratio $\kappa=4\times10^{-3}$ as in the experiments.

To represent the constant pressure in the sites occupied by the nonviscous displacing fluid, occupied sites in the growing cluster were selected at random with equal probabilities. This corresponds to boundary conditions in the dielectric breakdown model [16,20]. A particle was launched on a random-walk path from this site in the direction of a randomly selected nearest neighbor. Throughout the simulation the random walk was terminated if the particle returned to the aggregate. The particle could always leave the aggregate along a high-permeability bond, but it could leave along a low-permeability bond only with a probability proportional to the permeability ratio $\kappa<1$. If unsuccessful, the whole process started again.

When a particle was successfully launched on a random walk, it moved from one site to one of its nearest neighbors with probability P_i and so on. When the particle reached a site at the boundary of the model, the ran-

dom walk was stopped and the first unoccupied site entered by the particle on this trajectory was added to the cluster to represent growth of the viscous finger. Time-reversal arguments show that this scheme is equivalent to standard DLA where particles start at the boundary and end their trajectory at the aggregate [21]. This procedure was repeated until the aggregate reached the boundary of the model.

The algorithm described above requires large amounts of computer time. Usual methods to speed up simulations of this type, by making long steps far from the aggregate, cannot be used on the nonuniform model where the random-walk trajectory takes place. Also, the method is slow close to percolation since random walks on such structures have high fractal dimension [22,23].

V. RESULTS

A. Results of experiments and corresponding simulations

Figure 5 shows a photograph of an experiment at a given instance t. From this picture we find both the total mass $M(t)$ and radius of gyration $R_g(t)$. The solid circles in Fig. 6 show the result of analyzing a sequence of pictures. We obtain $M(R_g)$ as function of $R_g(t)$; the slope of the straight line fitted to these data is the radius of gyration dimension D_g of Eq. (8).

Each curve in Fig. 7 shows the number of air-filled pores or, equivalently, the displaced mass within circles of increasing radius R centered at the point of injection. The lowest curve is generated from a digitized image at an early stage of the displacement; the other curves each represent later instances in the same displacement experiment. The straight line is a fit to the last stage before breakthrough; its slope gives the cluster dimension D_c of Eq. (9). We estimate the error on both D_g and D_c to be ± 0.1. Changing the range over which we fit the straight line gives the main contribution to the error.

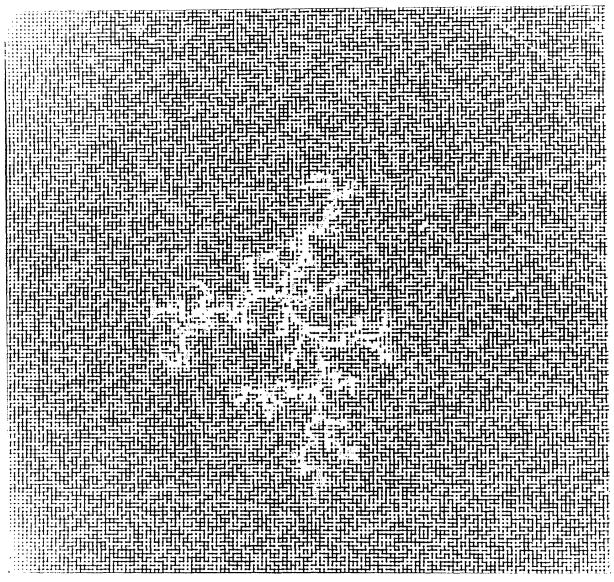

FIG. 5. Black glycerol fills pores and connecting bonds of the model. Areas blocked to flow appear white. Air injected through the central site has displaced glycerol, and these sites and bonds appear white.

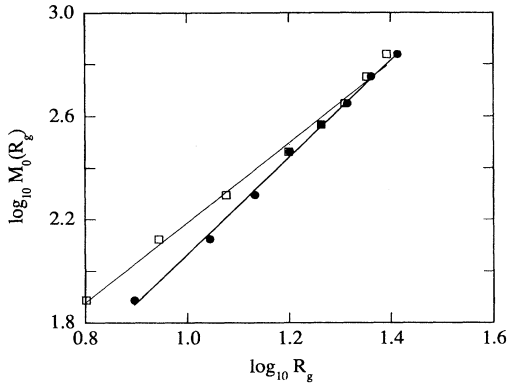

FIG. 6. Experiment and simulation. The number of pores $M(R_g)$ invaded by air as a function of the radius of gyration R_g for Ca=0.12. Solid circles are experimental data, and open squares are results of one simulation (the same as in Fig. 9) obtained as explained in the text. The solid lines show a fit to Eq. (8). In the range fitted the slopes are $D_g^{\text{expt}}=1.9$ and $D_g^{\text{sim}}=1.6$.

At a *given* value of R, the number of pores $M(R,t_1)$ invaded at one instance t_1 is less than at a later instance t_2, $M(R,t_1)<M(R,t_2)$. Thus in the interval t_2-t_1 new pores are added to the structure at radii $R<R_{\max}(t_1)$ and not only at values of R close to $R_{\max}(t_1)$. Qualitatively, this means that the structure in Fig. 7 appears to grow in the interior as well as at the tips. It is well established that DLA structures grow only at the tips [24].

We superimposed successive stages of the experiment as in Fig. 8, where pores added in each interval were assigned a different symbol. We found that the interior growth was an effect of the exact distribution of clusters of high-permeability bonds in the model. New pores

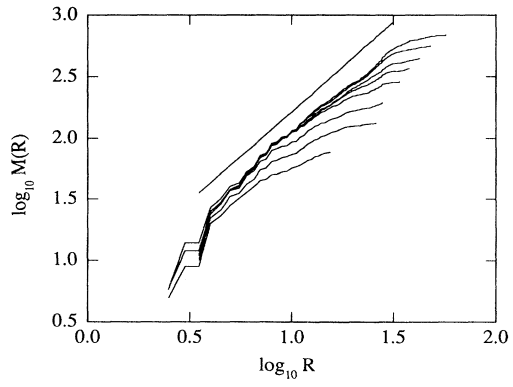

FIG. 7. Experiment. The cumulative mass $M(R)$ as a function of radius R for a sequence of stages of an experiment at Ca=0.12. The straight line is a fit to the last stage (shifted up for visibility) with slope $D_c=1.5$.

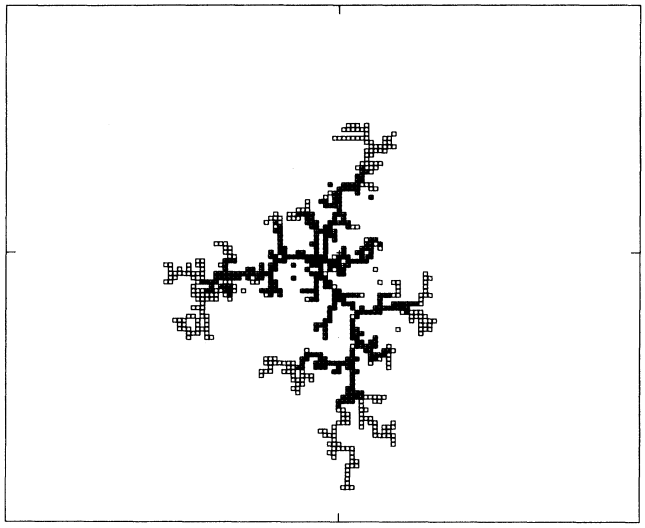

FIG. 8. Three experimental stages superimposed. Solid squares represent pores drained during the first 1.65 sec of the experiment, crossed squares represent pores drained during the next 1.65 sec, and open squares show those pores drained in the following 1.65-sec interval. A plus shows the site of injection.

were added predominantly at the tips of the three or four main arms of the aggregate. But some parts of the arms curl back or start out late and, indeed, contribute to the aggregate at radii $R < R_g(t)$, producing the layering of the curves in Fig. 7.

We performed simulations as described in Sec. IV B. The program returned a list of coordinates of sites (pores) belonging to the aggregate in the order in which they were added. To compare the simulation with experiments, we used the first $M_{\rm sim} = M_{\rm exp}(t_1)$ coordinates on the list and calculated the radius of gyration for the simulation at this stage. We also calculated $M(R)$ within circles of increasing radius between $a < R < R_{\rm max}(t_1)$ around the seed particle. Next, we used the first $M_{\rm sim} = M_{\rm exp}(t_2)$ and so on until we reached either the

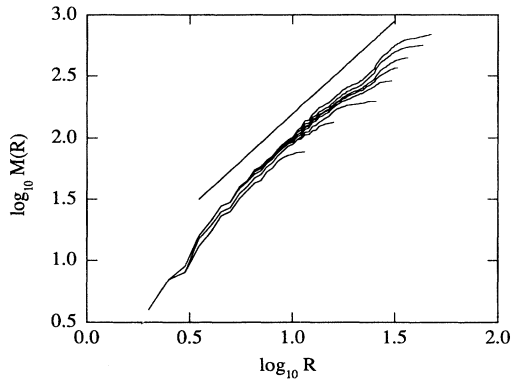

FIG. 9. Simulation. The cumulative mass $M(R)$ in one simulation as a function of the radius R for increasing values of the total cluster mass. The slope of the fitted line is $D_c = 1.5$ (shifted up for visibility).

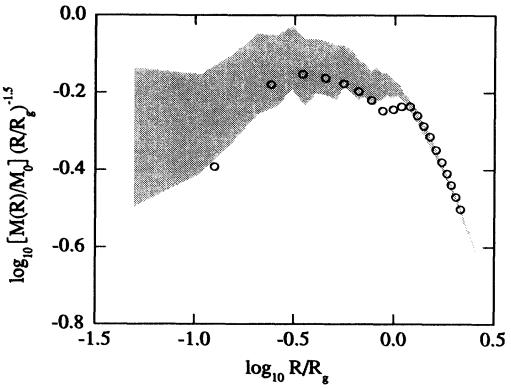

FIG. 10. Crossover function for experiment and simulations. Circles are experimental data showing the normalized mass $[M(R)/M_0](R/R_g)^{-1.5}$ as a function of the normalized radius R/R_g for the last stage of an experiment at Ca=0.12. The shaded gray region represents ten independent simulations on the experimental model. Results are averaged, and we only show the rms deviation of the simulations around the average.

maximum experimental mass or the maximum simulated "mass". This procedure allowed us to make plots such as the one in Fig. 9. As for the experimental data, these simulation data also approach the $M(R)$ curve for the largest cluster. The slope is $D_c \simeq 1.5 \pm 0.1$ for experimental as well as for these simulated data.

The crossover function $F(x)$ in Eq. (9), where $x = R/R_g$, is shown in Fig. 10 for the last experimental stage of the experiment (Ca=0.12) of Figs. 6 and 7. The plot emphasizes behavior at short length scales. The experimental data are shown together with the rms deviations around the average of ten independent simulations on the experimental model. The simulation results are averaged by coarse graining the data from all simulations. The abscissa is subdivided into suitable segments, and the average radius and average mass within each segment is found. The standard deviation within each segment is found, and the shaded gray band in Fig. 10 corre-

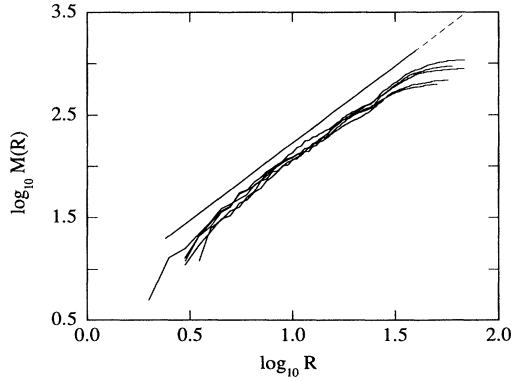

FIG. 11. Experiment. The cumulative mass $M(R)$ as a function of radius R for the last stage of five independent experiments. One experiment is done at Ca$\simeq$0.02, two experiments are done at Ca$\simeq$0.03, and two experiments are done at Ca$\simeq$0.12. The straight line is a fit to all data (shifted up for visibility) with slope $D_c = 1.5$.

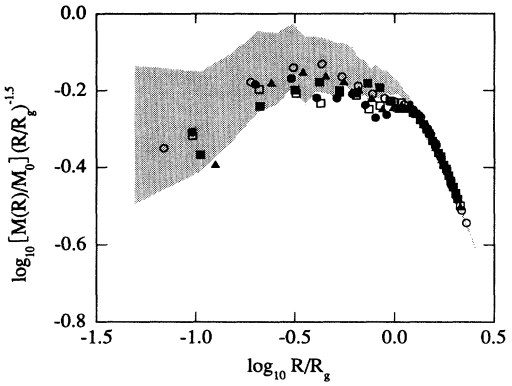

FIG. 12. Crossover function for experiment and simulations. The normalized mass $[M(R)/M_0](R/R_g)^{-1.5}$ as a function of the normalized radius R/R_g for the last stage of five experiments. Open circles, Ca$\simeq$0.02; solid circles and open squares, Ca$\simeq$0.03; and solid squares and triangles, Ca$\simeq$0.12. The shaded gray band represents ten independent simulations on the experimental model. Results are averaged, and we only show the rms deviation of the simulations around the average.

sponds to one standard deviation to either side of the average.

The results of other independent experiments on the same $f\simeq 0.50$ model but at different values of the capillary number $0.02\leq \mathrm{Ca}\leq 0.12$ are shown in Figs. 11 and 12. The simulations show variations that are larger than independent experiments on the same model.

Another way of comparing experiments and simulations is to find the amount of *geometrical* overlap at the same aggregate mass or at the same radius of gyration. For practical reasons we chose the first alternative, and an experiment-simulation overlap at the largest common aggregate mass M is shown in Fig. 13.

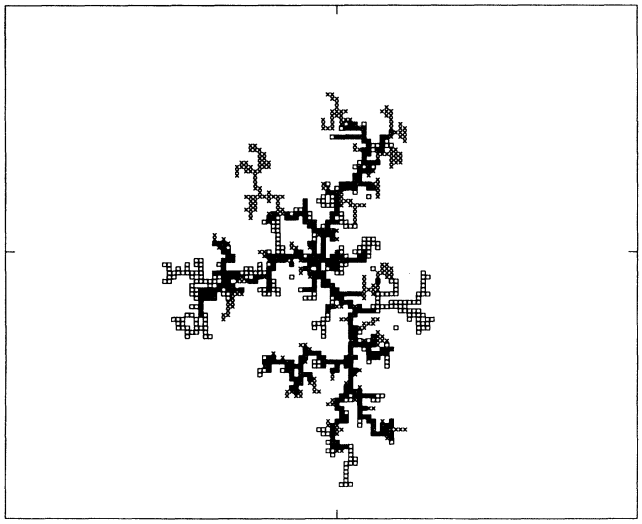

FIG. 13. Overlap of an experiment at Ca=0.12 and the simulation shown in Fig. 9. Experiment is shown in boxes, simulation crosses, and pores common to both in crossed boxes. Both experiment and simulation contain $M=690$ pores. The radii of gyration R_g are 25.9 and 24.7 in units of the lattice constant for the experiment and simulation, respectively.

TABLE I. Overlaps between aggregates obtained experimentally or in simulations. The *overlap* S is the pores shared by both structures (for example, by both experiment and simulation) divided by the mass at which they are compared. Comparison is made at the maximum common aggregate mass. When nothing else is stated, the error bar on the overlap is ± 0.05. The numbers given for the overlap of experiments with simulations are averages of S for one experiment with each of ten simulations. For simulation-simulation overlaps and experiment-experiment overlap, the number is the average of all combinations. The simulation-simulation overlap across different models is found by averaging overlaps for all combinations of one simulaton on each of nine different models with $f\simeq 0.50$ and $\kappa=4\times 10^{-3}$.

Overlap	$S=M_{\mathrm{overlap}}/M$	Fractal dimension D $\log_{10}M/\log_{10}R$
Experiment-simulation	0.55	1.5
Experiment-experiment	0.75±0.9	1.5
Simulation-simulation on identical models	0.52	1.5
Simulation-simulation Different models	0.16	1.5
On percolation cluster		
Oxaal *et al.* [15]		
Experiment-simulation	0.78	1.3
Simulation-simulation	0.79	1.3

A quantitative measure of the overlap is given by $S=M_{\mathrm{overlap}}/M$, where M_{overlap} is the number of pores common to experiment and simulation. The value of S given in Table I is the average overlap between experiment and ten independent simulations on the same model. Overlaps between two simulations may be defined similarly, and are also shown in Table I. Overlap between two experiments is not found at a common aggregate mass, since photographs cannot be taken at predetermined (and equal) aggregate masses. Therefore, we measure overlap between two experimental aggregates (mass M_1 and M_2) on the same model with the parameter $S=M_{\mathrm{overlap}}/M$, where $M=\min(M_1,M_2)$.

B. Simulation results on other network geometries

Figure 14 shows simulations on other realizations of 145×145 networks at $f\simeq 0.5$ and $\kappa=4\times 10^{-3}$. The top figure shows an average over nine models with four independent simulations on each. The middle and lower plots show two separate sets of four independent simulations, each set on a different model realization. The plots all show the crossover function $F(x)$ of Eq. (9), and although the average (over many realizations) $F(x)$ is constant for $x<1$, we observe that it has a model-dependent shape when we plot the simulations on different models separately.

C. Simulations on larger substrates

Figure 15 shows simulations on two larger models of 401×401 sites with $f\simeq 0.5$ and $\kappa=4\times 10^{-3}$. As in the

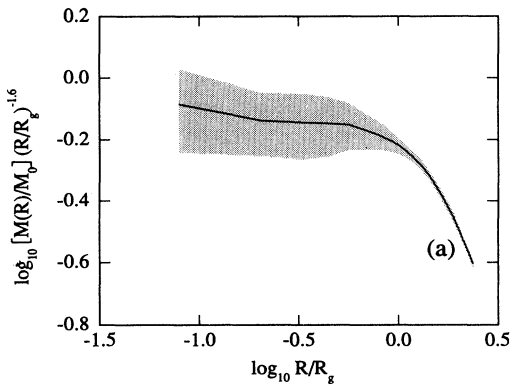

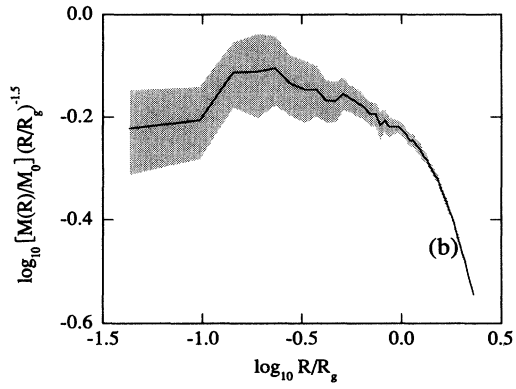

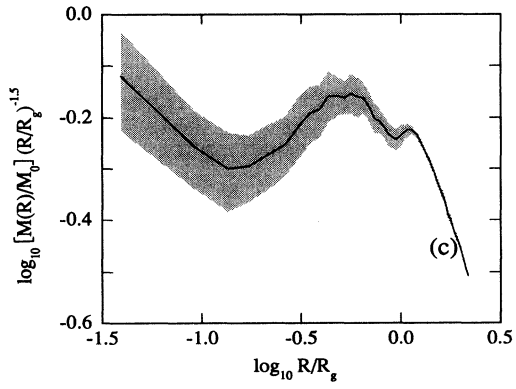

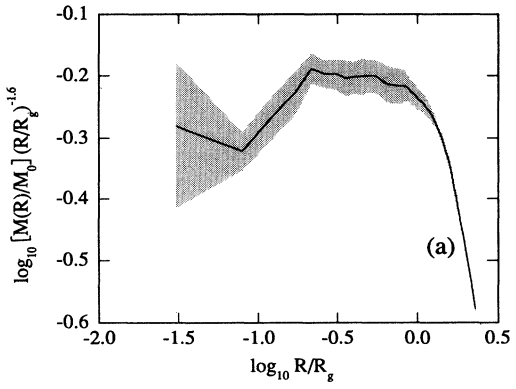

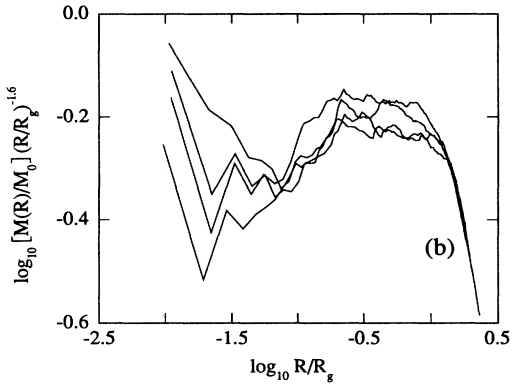

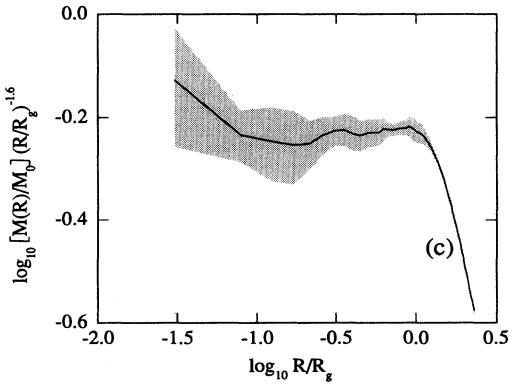

FIG. 14. Crossover function for simulations. The normalized number of pores $[M(R)/M_0](R/R_g)^{-1.6}$ as a function of the normalized radius R/R_g. Lines show average values; the shaded gray regions represent the rms deviation of the simulations around the average. (a) shows average of 36 independent simulations on nine *different* models. The permeability ratio was $\kappa=4\times10^{-3}$. Each model is a different realization of the case $f\simeq0.50$. (b) shows average and standard deviation for four independent simulations on *one* model. (c) shows average and standard deviation for four independent simulations on *another* model.

FIG. 15. Crossover function for simulations. The normalized number of pores $[M(R)/M_0(R/R_g)^{-1.6}$ as a function of the normalized radius R/R_g. Lines show average values; the shaded gray regions represent the rms deviation of the simulation around the average. (a) shows average of four independent simulations on a large 401×401 site model. The permeability ratio was $\kappa=4\times10^{-3}$ and $f\simeq0.50$. (b) shows the four independent simulations in (a). (c) shows average and standard deviation for four independent simulations on *another* 401×401 model.

previous section, we observe that the model geometry influences the shape of the crossover function $F(x)$ at length scales $R < R_g$. The average of these two sets of simulations scales as $D_c \simeq 1.6$.

VI. DISCUSSION

The two main quantities measured were the overlap of pairs of aggregates and the scaling of aggregates. We discuss and compare these quantities for aggregates generated in different manners.

A. Overlap

Overlap between independent experiments on the same model is high, $S=0.75$, and well above the overlap between experiments and "simulations on the experimental model," $S=0.55\pm0.05$. The latter value is the same as for overlap between two independent simulations on any (single) model realization $S=0.52$. The value of these overlaps are high compared to $S=0.16$ for overlap between simulations done on separate model realizations at $f \simeq 0.50$ and $\kappa=4\times10^{-3}$. We conclude that the underlying (percolation) geometry of the pore space strongly influences the growth of both the viscous fingers and simulations.

Experiments are more reproducible than simulations, as shown by S for these two cases. Lower simulation-simulation overlap could originate in the random walk, which adds a stochastic element in simulations responsible for added noise (as demonstrated by a lower overlap). Another source of noise in DLA stems from the stepwise growth of the aggregate. Every time a particle is added, the structure changes since it grows by one pore, whereas in VF growth occurs in several places simultaneously. In the future one could reduce experimental noise by working with more perfect models and reduce numeric "noise" by adding noise reduction [25] to the algorithm.

Early stages of overlap between experiments and simulations show that pores unique to the experiments are predominantly found at tips of the aggregate, while pores uniquely chosen by the simulation lie closer to the center. A similar observation [15] was made in VF on a percolation cluster.

B. Scaling

Scaling analysis of experimentally and numerically grown aggregates in Sec. V A shows that experiments and the average of ten independent simulations on the experimental model scale with the cluster dimension [Eq. (9)] $D_c=1.5\pm0.1$; this is shown in Figs. 7, 9, and 10. This value agrees with numerical results on larger models at $\kappa=0.002$ and $f \simeq 0.50$ by Meakin *et al.* [14]. We have done 58 independent simulations on 10 model realizations of size 145×145 sites ($f \simeq 0.50$, $\kappa=0.004$). Averaging over all simulations, we find an exponent $D_c=1.6\pm0.1$, which also is what we find for eight independent simulations on two models of size 401×401.

Before discussing the scaling relations in more detail, it is appropriate to comment on the range of length scales over which we find geometric scaling behavior. To establish the fractal nature of a random structure and determine its characteristic dimension(s), geometric scaling should be measured over a wide range of length scales. The total range of length scales we have at our disposal is set by the model. It is about two orders of magnitude since our model size $L=145$. As discussed in the sections on design, production, and digitization, the present models are close to the limit of what may be experimentally achieved.

However, the range over which we can expect to study, geometric scaling is reduced for the following reasons: The minimum of the range is set by the experimentally obtainable minimum size of the aggregate, which was $R_{\min} \simeq 3-5$ lattice constants. Likewise, the maximum of the range is set by the largest length where aggregates show a power-law behavior, i.e., R_g. In our model $R_{\max}=102a$, and the range over which we may test scaling is $\log_{10}R_g \in [0.4, 1.8]$. However, since we have a record of how the structure develops, we may extrapolate the scaling of viscous fingers from the asymptotic approach of $M(R)$ curves for early stages of displacement to the $M(R)$ curve for the last stage as Figs. 7 and 9 show.

As discussed in Sec. V A, the experimental $M(R)$ curves in Fig. 7 show a layered structure, and we argued that this appearance is produced by interior growth in the aggregate. Interior growth are drained pores added to the aggregate at radii $R < R_g(t_1)$ in an interval that *starts* at time t_1. About 70% of our *simulations* show interior growth. In contrast to our experiments and simulations, it has been established that DLA aggregates grow in an active zone outside R_g [24], have low growth probabilities "inside" the aggregate [26], and that their growth is realized on a set of points of fractal dimension one [27].

C. Relation between D_c and D_g

The radius of gyration dimensions D_g for experiment and simulations differ by 0.33 (see Fig. 6). This result is surprising since the cluster dimensions D_c are practically the same for these two sets of data. Most of the difference originates in the large shift $\Delta_{\text{expt}}=D_g-D_c=0.42$ between these two fractal dimensions for the experimental aggregate. We find that D_g and D_c are related as Fig. 16 shows. Each $M(R)$ *curve* is mapped onto a *point* $M(R_g)$, where the *total* mass of a given stage is plotted at the radius of gyration. The early experimental stages are stringy; i.e., R_g is large compared to the mass of the aggregate. As the aggregate grows, mass is added in the *interior* of the aggregate as well as at radii larger than R_g, as discussed above. The points added in the interior of the aggregate contribute little toward increasing R_g, while the total mass increases regardless of where new mass is added. Thus the slope of the curve $M(R_g)$ becomes steeper.

In contrast, the simulated aggregate of Fig. 9 maintains its radial mass distribution unchanged as it grows, and $\Delta_{\text{sim}} \simeq 0.03$ is much smaller than for the experiment. It is also smaller than the error on the fractal dimension.

Two other experiments have been analyzed similarly and also show a large difference between D_c and D_g.

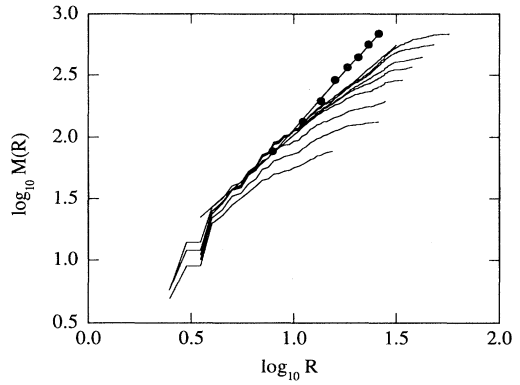

FIG. 16. Experiment. The cumulative mass $M(R)$ as a function of radius R for a sequence of stages of the experiment at Ca=0.12. A straight line is fitted to the last stage with a slope $D_c=1.5$, but is not shown. Solid circles represent the total mass at each stage placed at the radius of gyration of the aggregate at that stage. The straight line is a fit to these points and has a slope $D_g=1.9$.

Other simulations than the one used in Figs. 6 and 9 exhibit internal growth and an associated large Δ, while simulations that show no obvious internal growth have small Δ's. We estimate that average differences are $\Delta\simeq 0.3$ for large shifts and $\Delta\simeq 0.1$ for small shifts; the latter cannot be distinguished from the error on the fractal dimensions.

We draw attention to a difference in boundary conditions used in our simulations and the usual rule in large-scale DLA-like simulations [12,28]. In our simulations the model has a given size L, and as the aggregate grows, the distance between the tips of the longest arms and the boundary shrinks, thereby causing the growth probablity to diverge. In large-scale simulations it is usual to move the outer boundary—equivalent to increasing L as the aggregate grows—thus preventing the divergence mentioned above. The lack of divergence as the aggregate approaches the boundary is unphysical for VF; ∇P *does* diverge and we *do* observe a large increase in the growth velocity of the viscous fingers near the boundary. We believe that the different boundary conditions explain why Feder *et al.* [18] find the cluster dimension of viscous fingers to be systematically smaller than for standard DLA. Simulations employing static boundary conditions were used by Meakin [28] and Måløy *et al.* [21], but unfortunately the effect on the cluster dimension was not discussed.

D. Crossover functions

Experiments and "simulations on the experimental model" correspond beyond merely scaling with the same cluster dimension $D_c\simeq 1.5$ and having a high overlap $S=0.55$: The crossover function $F(x)$ [Eq. (9)] plotted in Fig. 12 shows that in the range $R\leq R_g$ experimental data almost entirely fall within plus minus one standard deviation around the average of ten independent simulations on the model. Repeated and independent simulations on the other models with $f\simeq 0.50$ and $\kappa=0.004$ show that the model strongly influences the details of the crossover function $F(x)$ at length scales $R\leq R_g$, as shown in Figs. 14(b) and 14(c).

Variations in $F(x)$ on different models are more pronounced than differences between experiment and simulations on the experimental model. Clearly, the inhomogeneous cluster structure of the model influences the growth of the aggregate, also as expressed in details of scaling. Figure 15 shows that, also in 401×401 models, simulations at $R<R_g$ scale in a way that is typical for the model geometry.

We believe that the dependence on model geometry may be explained by paths drained (or sites visited) during early stages of aggregate growth. Here clusters (of pores connected by good bonds) used for further growth are chosen; also the pores at which the chosen clusters are entered decide main features of the paths that will be followed. When the aggregate is small, all paths to the boundary are equivalent *except* for the local difference in permeability close to the aggregate surface. Therefore, for many network realizations at $f\simeq f_c=0.50$, the details of the placement of the two types of bonds near the injection (or seed) site will influence aggregate growth decisively. These details of the aggregate are reflected in the behavior of the crossover function at $R<R_g$.

As discussed in Sec. II B, Meakin *et al.* [14] suggest the existence of a crossover length $L_\kappa=A\kappa^{-\alpha}$ (where $\alpha\simeq 0.25$ and A is the unknown amplitude), set by the bond permeability ratio. The idea is that, if $\kappa=0$, the low-permeability bonds are closed and we have a lattice with bond percolation, while $\kappa=1$ gives us an ordinary square lattice with all bonds present and equal so that we have a square-lattice model; i.e., L_κ will change from infinity to A.

Aggregates grown on these geometries have known scaling exponents $D=1.3$ and 1.7, respectively, and somehow the behavior must go from one to the other as κ is changed.

Since we find crossover functions (Figs. 14 and 15) that depend strongly on model geometry, this shows that $L_\kappa\leq L$, for if $L_\kappa\ll L$, we would see the characteristic scaling of DLA independent of the lattice geometry [29]. Our experiments are also drastically different from experiments on a percolation cluster [15]. We do not see $D_c=1.3$, and we may conclude that L_κ is not $\gg L$. So we may give a rough estimate: $L_\kappa=A\kappa^{-\alpha}=0.5L$ and find $A\simeq 0.125L\simeq 18a$.

Repeated experiments on the same model, where some were done at lower capillary number, i.e., lower displacement pressure, all scale with the same exponent and have very similar crossover functions $F(x)$ (see Figs. 11 and 12). Thus all our experiments seem to be quite equal and lie in the VF domain [6]. However, experiments at Ca$\simeq$0.03 and 0.02 have higher mass at breakthrough than experiments at Ca$\simeq$0.12, $M_{0.02}\simeq 1.5M_{0.12}$. We believe this to be the first sign of the continuous transition to capillary fingering [6]. It is interesting to note that scaling is not noticeably affected.

E. Relation to work of other authors

Chen and Wilkinson [4] and Lenormand, Touboul, and Zarcone [6] have previously studied two-fluid displacement in two-dimensional porous network models by combining experiments and numerical methods. Compared to our work, there are three main areas of difference: model geometry, the algorithm used in simulations, and method used to compared experiment and simulation.

The model we have used is inhomogeneous, as discussed in Sec. II A, whereas the other groups used homogeneous models. We used a statistical or cellular automat-type algorithm on a model that has exactly the same cluster geometry as the experimental network. The two other groups solve the flow equations deterministically, on models that are only statistically similar to the experimental models, and also take surface tension and capillary pressure (which are neglected in our simulations) into account [6]. Finally, we have been in a position where we could compare experimental results and numerical results in great detail, whereas the other groups just have had statistical methods available. As we do here, they find a good agreement between experiment and simulations. However, the deterministic methods used by the other groups are very demanding and expensive compared with the extended DLA algorithm of Meaking *et al.* [14] that we have used, and one of our main points has been to check the validity of the simple extended DLA algorithm on a complex pore-space geometry.

VII. CONCLUSIONS

We have presented a method to compare model experiments and simulations in detail and have used it to study the displacement of a high-viscosity fluid by a low-viscosity fluid at high capillary numbers in well-defined *inhomogeneous* networks.

Previously, in a system where the pore space had a percolation-cluster geometry [15], the displacement front was found to be fractal, with dimension $D=1.3$. It was confined to the percolation cluster backbone that strongly influenced the aggregate formed in the displacement.

In the present models the pore-space percolation geometry was modified by adding low-permeability bonds, and the displacement-front geometry was strongly changed. The effective fractal dimension was $D_c \simeq 1.5$, and crossover phenomena occurred, as expressed by $D_g \neq D_c$. We suggest that the difference between the cluster dimension D_c and radius of gyration dimension D_g may be used as a measure of the degree of internal growth in a structure.

The permeability of the thin bonds $\kappa=0.004$ was high in the sense that we cannot regard their presence as a small perturbation away from critical percolation. Therefore, we find the strong influence of the model geometry on the front structure [as expressed in the crossover function $F(x=R/R_g)$, the high overlap, and the interior growth], both remarkable and important.

The simple modified DLA algorithm of Meakin *et al.* [14] described the observed front well and also showed the dependence on detailed pore geometry observed in the experiments.

ACKNOWLEDGMENTS

I want to thank J. Feder and T. Jøssang for continuing support, advice, and many stimulating discussions. I also want to thank P. Meakin and A. Aharony for their interest and for helpful and stimulating discussions. Computers have been used at every stage of this work, and others have generously provided most of the programs needed. They are as follows: F. Boger (mask production and the demanding programs to digitize and extract data from experimental photographs), P. Meakin (simulations), and J. Feder (data analysis and fitting). I thank them all. I also thank G. Holm for photographic work and V. Frette, E. Hinrichsen, and all other colleagues for comments and help. I gratefully acknowledge support by VISTA, a research cooperation between the Norwegian Academy of Science and Letters and Den norske stats oljeselskap a.s. (STATOIL), and by NAVF, the Norwegian Research Council for Science and the Humanities.

[1] B. B. Mandelbrot, *Fractals: Form, Chance, and Dimension* (Freeman, San Fransisco, 1977).
[2] J. Feder, *Fractals* (Plenum, New York, 1988).
[3] T. Viscek, *Fractal Growth Phenomena* (World Scientific, Singapore, 1989).
[4] J. D. Chen and D. Wilkinson, Phys. Rev. Lett. **55**, 1892 (1985).
[5] K. J. Måløy, J. Feder, and T. Jøssang, Phys. Rev. Lett. **55**, 2688 (1985).
[6] R. Lenormand, E. Touboul, and C. Zarcone, J. Fluid Mech. **189**, 165 (1988).
[7] J. Bear and Y. Bachmat, *Introduction to Modeling of Transport Phenomena in Porous Media* (Kluwer Academic, Dordrecht, 1990).
[8] A. Zaitoun, F. Kalaydijan, and C. Jaquin, in *Fundamentals of Fluid Transport in Porous Media,* Proceedings of the Fifth IFP Conference on Exploration and Production, Arles, France, 1990, edited by F. Kalaydijan (IFP, Paris, 1991).
[9] L. Paterson, Phys. Rev. Lett. **52**, 1621 (1984).
[10] J. D. Sherwood and J. Nittman, J. Phys. (Paris) **47**, 15 (1986).
[11] J. D. Sherwood, J. Phys. A **19**, L195 (1986).
[12] T. A. Witten and L. M. Sander, Phys. Rev. Lett. **47**, 1400 (1981).
[13] L. Paterson, J. Fluid Mech. **113**, 513 (1981).
[14] P. Meakin, M. Murat, A. Aharony, J. Feder, and T. Jøssang, Physica A **115**, 1 (1989).
[15] U. Oxaal, M. Murat, F. Boger, A. Aharony, J. Feder, and T. Jøssang, Nature **329**, 32 (1987).
[16] L. Niemeyer, L. Pietronero, and H. J. Wiesmann, Phys. Rev. Lett. **52**, 1033 (1984).

[17] M. Murat and A. Aharony, Phys. Rev. Lett. **57**, 1875 (1986).
[18] J. Feder, E. L. Hinrichsen, K. J. Måløy, and T. Jøssang, in *Fractals in Physics,* edited by A. Aharony and J. Feder (North-Holland, Amsterdam, 1989), pp. 104–111,
[19] M. P. M. den Nijs, J. Phys. A **12**, 1857 (1979).
[20] M. Murat and A. Aharony, Phys. Rev. Lett. **58**, 2503 (1987).
[21] K. J. Måløy, F. Boger, J. Feder, T. Jøssang, and P. Meakin, Phys. Rev. A **36**, 318 (1987).
[22] S. Alexander and A. Orbach, J. Phys. (Paris) Lett. **43**, L625 (1982).
[23] D. Stauffer, *Introduction to Percolation Theory* (Taylor & Francis, London, 1985).
[24] M. Plischke and Z. Rácz, Phys. Rev. Lett. **53**, 415 (1984).
[25] J. Nittmann and H. E. Stanley, Nature **321**, 663 (1986).
[26] B. B. Mandelbrot and C. J. G. Evertz, Nature **348**, 143 (1990).
[27] K. J. Måløy, F. Boger, J. Feder, and T. Jøssang, in *Time-Dependent Effects in Disorderd Materials,* edited by R. Pynn and T. Riste (Plenum, New York, 1987), pp. 111–138.
[28] P. Meakin, in *Time-Dependent Effects in Disordered Materials* (Ref. 27), pp. 45–70.
[29] When doing simulations. In experiments we know we get "snowflakes" with fourfold geometry.